GDCh Research Article Angewandte International Edition Chemie www.angewandte.org

How to cite: *Angew. Chem. Int. Ed.* **2025**, *64*, e202415642
doi.org/10.1002/anie.202415642

CO_2 Reduction

Atmosphere Induces Tunable Oxygen Vacancies to Stabilize Single-Atom Copper in Ceria for Robust Electrocatalytic CO_2 Reduction to CH_4

Fang Huang[+], Xiangyu Chen[+], Huanhuan Sun, Qingduo Zeng, Junjie Ma, Dong Wei, Jinliang Zhu, Zhengjun Chen, Taoyuan Liang, Xucai Yin, Xijun Liu, Jing Xu, and Huibing He**

Abstract: Electrochemical carbon dioxide reduction (ECO_2RR) shows great potential to create high-value carbon-based chemicals, while designing advanced catalysts at the atomic level remains challenging. The ECO_2RR performance is largely dependent on the catalyst microelectronic structure that can be effectively modulated through surface defect engineering. Here, we provide an atmosphere-assisted low-temperature calcination strategy to prepare a series of single-atomic Cu/ceria catalysts with varied oxygen vacancy concentrations for robust electrolytic reduction of CO_2 to methane. The obtained Cu/ceria catalyst under H_2 environment (Cu/ceria-H_2) exhibits a methane Faraday efficiency (FE_{CH4}) of 70.03 % with a turnover frequency (TOF_{CH4}) of 9946.7 h^{-1} at an industrial-scale current density of 150 mA cm^{-2} in a flow cell. Detailed studies indicate the copious oxygen vacancies in the Cu/ceria-H_2 are conducive to regulating the surface microelectronic structure with stabilized Cu^+ active center. Furthermore, density functional theory calculations and operando ATR-SEIRAS demonstrate that the Cu/ceria-H_2 can markedly enhance the activation of CO_2, facilitate the adsorption of pivotal intermediates *COOH and *CO, thus ultimately enabling the high selectivity for CH_4 production. This study presents deep insights into designing effective electrocatalysts for CO_2 to CH_4 conversion by controlling the surface microstructure via the reaction atmosphere.

1. Introduction

Electrochemical carbon dioxide reduction (ECO_2RR) to produce valuable chemicals and fuels helps to alleviate the energy crisis in the carbon-neutral context.[1] Methane (CH_4) is a CO_2 reduction product with significant application value in the chemical industry.[2] With its high combustion ratio, CH_4 can substitute other fossil fuels for generating heat and electricity,[3] and its liquid form can power the SpaceX Starship into the outer space. Copper-based catalysts are the main metal materials that can reduce CO_2 to hydrocarbons with a considerable turnover frequency.[4] Several strategies have been discovered to reduce CO_2 to CH_4 for Cu-based electrocatalysts,[5] including controlling the catalyst morphology,[6] engineering the interface,[7] adjusting the oxidation state,[8] constructing heterojunctions,[9] and adopting Cu single-atom catalysts.[10] However, most of them exhibit low selectivity, poor current density, and inferior conversion rates, especially under high current required for industrial applications.[11] Therefore, developing superior copper-based catalysts is appealing yet challenging at the current stage.

Single-atom catalysts (SACs) with atomic dispersion sites display exceptional catalytic activity due to their maximum atomic utilization and unique electronic structure,[12] which has been widely used in ECO_2RR.[10c,13] Besides, SACs are distinguished by the designability of metal-support interactions and coordination environments at the atomic scale.[14] So far, carbonaceous materials such as organometallic metal frames and carbon nanotubes are the most common supports for SACs, which can stabilize the atomic sites of SACs and avoid the excessive charge transfer.[13,15] However, due to their inherent properties, the carbon-based materials shows weaknesses in the chemical and thermal stability.[16] Hence, it is necessary to explore other materials as carriers to disperse SACs for ECO_2RR.

As a wide range of rare earth oxides, ceria is a good support that have been used in diverse catalytic reaction,[17] such as supercapacitor,[18] water-gas shift,[19] ammonia oxidation,[20] and CO_2 reduction.[21] The selectivity of CO_2 reduction to CH_4 in the ECO_2RR process depends on the activation degree of CO_2 molecules and the adsorption

[*] F. Huang,[+] X. Chen,[+] H. Sun, Q. Zeng, J. Ma, D. Wei, J. Zhu, Z. Chen, T. Liang, X. Yin, X. Liu, Prof. J. Xu, Dr. H. He
Guangxi Key Laboratory of Petrochemical Resource Processing and Process Intensification Technology, Guangxi Key Laboratory of Electrochemical Energy Materials, School of Chemistry and Chemical Engineering
Guangxi University
Nanning 530004, PR. China
E-mail: xujing@ecust.edu.cn
huibinghe@gxu.edu.cn

Prof. J. Xu
State Key Laboratory of Green Chemical Engineering and Industrial Catalysis, School of Chemical Engineering
East China University of Science and Technology
Shanghai 200237, PR. China

[+] These authors contributed equally to this work.

intensity of key intermediates (such as *COOH),[22] which is of major challenge, and therefore necessitates appropriate adjustment to the surface electronic structure of the metal active sites.[10c,15b,23] In view of this, introducing tunable oxygen vacancy defects on ceria support is an effective approach, as oxygen vacancies can get an uncoordinated number of the metal active sites. For example, Kshirodra et al. demonstrate that a higher oxygen vacancy concentration on Cu/CeO_2 catalysts resulted from more available Cu^+ sites achieves a FE_{CH4} of 42 %.[10a] Furthermore, nanocrystalline Cu/CeO_{2-x} by double-tooth adsorption of Cu and CeO_{2-x}O-vacancy can stabilize ECO_2RR intermediates,[7b] which produce a FE_{CH4} of 54 % at −1.2 V versus reversible hydrogen electrode (RHE). However, the controllable regulation of oxygen vacancy concentration to develop high-performance catalysts remains to be elucidated. Moreover, the correlation between oxygen vacancy concentration and the electrocatalytic efficacy of ceria-based catalysts is worth of in-depth study.

Here, we reported a series of Cu/ceria catalysts with manipulated oxygen vacancy concentration through low-temperature annealing under variable reaction atmospheres (air, Ar and H_2). The differences in the number of oxygen vacancies on the catalyst under three calcination environments were demonstrated by the Electron paramagnetic resonance (EPR), Raman spectroscopy, and X-ray photoelectron spectroscopy (XPS). The X-ray absorption near-edge structure (XANES) confirms the monatomic structure of the Cu/ceria-H_2 catalyst, and the main valence state of Cu was +1. Compared to the Cu/ceria-Air and Cu/ceria-Ar, the Cu/ceria-H_2 catalyst owns the highest number of oxygen vacancies, helping to stabilize more active Cu^+. As a result, the oxygen vacancy-rich Cu/ceria-H_2 exhibits a high FE_{CH4} of 70.03 % at −1.49 V vs RHE, far exceeding the counterparts of Cu/ceria-Air (47.11 %) and Cu/ceria-Ar (39.91 %). Operando attenuated total reflectance surface-enhanced infrared absorption spectroscopy (ATR-SEIRAS) and theoretical calculations indicate that the oxygen vacancies can enhance the degree of CO_2 activation and the adsorption of key intermediates (*COOH and *CO), thus promoting the charge transfer kinetics and methane production rate. This work presents valuable insights into the controllable regulation of oxygen vacancies at the atomic level to achieve efficient CO_2 electrolysis to CH_4.

2. Results and Discussion

2.1. Material Synthesis and Characterization

The synthetic Scheme of Cu/ceria catalysts with different oxygen vacancy concentrations was presented in Figure 1a. First, the ceria precursor was prepared by a hydrothermal method using NaOH and $Ce(NO_3)_3$ as the reactants.[7a] The diffraction peaks match well with the face-centered cubic-fluorite ceria structure (JCPDS: 43–10102) (Figure S1). As shown in the scanning electron microscope (SEM) and transmission electron microscope (TEM) images, the ceria precursor consists of many small nanorods that can be easily

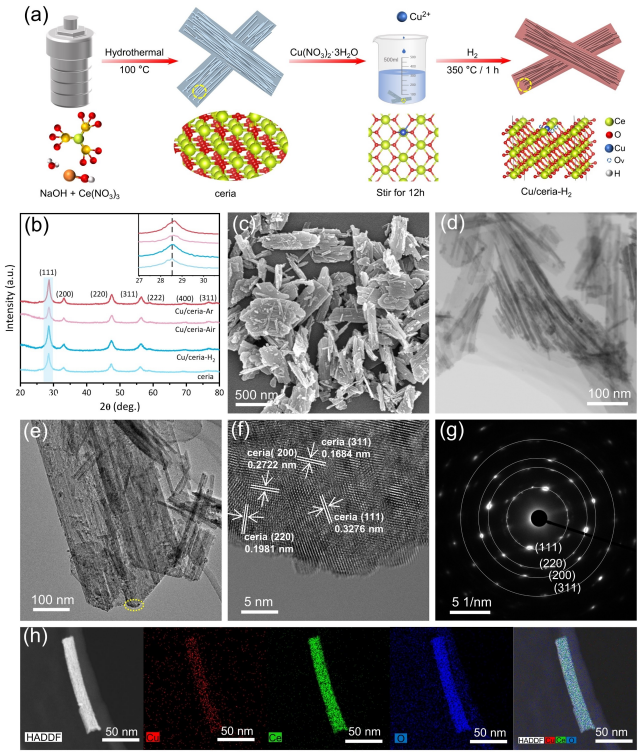

Figure 1. Materials preparation and physical characterizations. (a) Schematic illustration for the synthesis of Cu/ceria-H_2 catalyst. (b) XRD patterns of different Cu/ceria catalysts. (c) SEM images of Cu/ceria-H_2 catalyst. (d–e) TEM and (f) HR-TEM images of Cu/ceria-H_2. (g) The corresponding SAED pattern of Cu/ceria-H_2. (h) HAADF-TEM and EDS elemental mapping images of Cu/ceria-H_2 catalyst.

aggregated into nanosheets (Figure S2). Then, the Cu/ceria catalysts were obtained by calcination the ceria precursor under different atmospheres with the addition of copper salts. The XRD patterns of the Cu/ceria samples were shown in Figure 1b. The (111) crystal plane of the Cu/ceria catalyst showed a slight shift to a higher Bragg angle with increasing Cu content compared to pure ceria (Figure 1b, inset), which was consistent with the Cu content quantified by ICP-OES (Table S1). This could be explained by the incorporation of Cu^{2+} ions into the ceria lattice, to replace small Ce^{4+} ions with large Cu^{2+} ions, leading to a decrease in the lattice parameters and lattice expansion.[8]

SEM images shows that copper-supported ceria catalysts have similar structural characteristics to ceria, indicating that the atmosphere-assisted calcination process has little effect on the materials morphology (Figure 1c and Figure S3). In TEM and HR-TEM images (Figures 1d and 1e), individual Cu nanoparticles or Cu species-related lattice fringe were not observed in the Cu/ceria-H_2 catalyst, indicating that Cu species are highly dispersed in ceria, particularly due to the very little amount of Cu resource or in its monatomic form.[10a] Besides, the HR-TEM images (Figure 1f) displays that the lattice spacings of the ceria (311), (111), and (220) crystal faces become larger after loading with Cu, indicating an expansion of the ceria host

lattice. The selected area electron diffraction (SAED) result was consistent with the XRD pattern (Figure 1g).

Furthermore, the high-angle annular dark-field transmission electron microscopy (HAADF-TEM) and the energy dispersive X-ray spectroscopy (EDS) elemental map reveal a uniform distribution of Cu, Ce, and O species, without the observed aggregation on the three Cu/ceria catalysts (Figure 1h and Figure S4–S6). The nitrogen adsorption-desorption isotherms of Cu/ceria samples were shown in Figure S7a, where the Brunner–Emmet–Teller (BET) specific surface area of Cu/ceria-H_2 (97.2 m^2/g) was slightly larger than that of Cu/ceria-Air (94.5 m^2/g) and Cu/ceria-Ar (93.1 m^2/g). The related pore size (~20 nm) distribution in Figure S7b suggests the mesopores were produced in the calcination procedure for the Cu/ceria under different reaction atmosphere. In addition, Figure S8 displayed the size distributions of the three catalysts. Among the three catalysts, the Cu/ceria-H_2 has a smallest size with a diameter of 7.32 ± 0.19 nm and a length of 132.12 ± 3.88 nm. The small diameter of Cu/ceria-H_2 along with high BET specific surface area may facilitate the rapid adsorption of CO_2 to the saturation state, enabling the subsequent catalytic reaction.

X-ray photoelectron spectroscopy (XPS) was used to examine the oxygen deficiency and characterize the chemical valence states of the elements. The carbon spectra were calibrated by 284.80 eV of the C1s spectrum after charge compensation (Figure S9a).[24] The XPS full spectra of the three Cu/ceria samples were presented in Figure S9b, revealing the presence of Cu, Ce, O, and C elements. The Ce 3d XPS spectrum was simulated to synthesize ten peaks. The six peaks associated with Ce^{4+} can be found at 882.68 eV (V), 889.21 eV (V“), 898.5 eV (V”), 901.22 eV (U), 907.66 eV (U“), and 916.94 eV (U”).[10b] The Ce^{3+} peaks were located at 880.72 eV (V_0), 885.54 eV (V′), 898.80 eV (U_0), and 903.60 eV (U′) (Figure 2a). The ratio of peak areas for Ce^{3+} and Ce^{4+} revealed the Cu/ceria-H_2 catalyst has the highest Ce^{3+} content (Table S2).[10b] It is worth mentioning that pure ceria has a higher content of Ce^{3+} compared to Cu/ceria, because another Ce^{3+} was oxidized and converted to Ce^{4+} when Cu^{2+} replaces the Ce^{3+} adjacent to the oxygen vacancy.[10b] Thus, an increase in Cu^{2+} doping leads to a decrease in the ratio of Ce^{3+}/Ce^{4+} in comparison to the original pure ceria. The high electrocatalytic performance of Cu/ceria catalysts is often attributed to the presence of oxygen vacancies.[7b,10a] Additionally, the O 1s XPS spectra were separated into three peaks (Figure 2b), representing lattice oxygen (O_L) at 529.59 eV, chemisorbed oxygen (O_v) at 531.69 eV, and surface oxygen (O_{Sur}) at 533.21 eV, respectively.[14] O_L, O_v and O_{Sur} correspond to O^{2-},O_2^{2-} and O_2^- ions, in which the peak area of O_v can quantify the existence of oxygen vacancies.[25] Obviously, Cu/ceria-H_2 catalyst features more oxygen vacancies compared to the other catalysts (Table S3). The formation of oxygen vacancies was the transfer of electrons to Ce^{4+} by oxygen ions accompanied by the formation of Ce^{3+} ions to maintain electrical neutrality, so that the concentration of oxygen vacancies was consistent with the content of Ce^{3+} (Figure 2c).[7b]

The Raman spectra of the different catalysts further elucidate the structural defects of the obtained Cu/ceria catalysts. As shown in Figure 2d, the spectra display major bands at 255, 456, and 600 cm^{-1}, respectively. The peak at 255 cm^{-1} belongs to the second-order transverse acoustic (2TA) propagation mode. The peak at 456 cm^{-1} was the triple degenerate mode (F_{2g}) linked to the symmetrical stretching oscillations of the O^{2-} neighboring the Ce^{4+}. The defect induction mode (D) peak near 600 cm^{-1} could be assigned to the presence of oxygen vacancies. The concentration of oxygen vacancy defects in catalysts can be quantitatively measured by the relative intensity of D and F_{2g}, which is denoted as I_D/I_{F2g}.[26] All the Raman peaks of Cu/ceria catalysts are slightly more noticeable than pure ceria at around 600 cm^{-1}, indicating the presence of oxygen vacancies in the Cu/ceria catalyst. The degree of I_D/I_{F2g} proportionate to the structural defects follows the sequence of Cu/ceria-H_2 > Cu/ceria-Air > Cu/ceria-Ar (Figure S10), proving that the Cu/ceria-H_2 has the richest oxygen vacancies.[27] Electron paramagnetic resonance (EPR) analysis was used to further compare the oxygen vacancies of the three Cu/ceria catalysts treated with different atmospheres. The peak of oxygen vacancy at $g = 2.003$ was observed, with the highest intensity detected in the Cu/ceria-H_2 catalyst (Figure 2e**)**. The quantitative analysis results of EPR also showed that Cu/ceria-H_2 has the highest oxygen vacancy concentration, followed by Cu/ceria-Air and Cu/ceria-Ar (Table S4). The above spectroscopic studies collectively corroborate the feasibility of atmosphere treatment in adjusting the oxygen vacancy concentration in the Cu/ceria catalyst samples.

Figure S11a showed the XPS spectra of Cu 2p in Cu/ceria catalysts synthesized at different calcination atmosphere. The characteristic present at 930.0 eV corresponds to Cu^0 or Cu^+, and the peak of 933.2 eV corresponds to Cu^{2+}, which may be due to the inevitable oxidation during the experiment.[7d,28] Although it was difficult to distinguish the Cu^0 or Cu^+ from the Cu 2p core level spectrum, the peak of the LMM-Auger spectrum at 916.5 eV confirms the presence of the Cu^+ signature (Figure S11b).[10a] The Cu^+ was present in three Cu/ceria catalysts, and Cu/ceria-H_2 owned the highest Cu^+ number, followed by Cu/ceria-Air and Cu/ceria-Ar (Figure S12). Interestingly, the content of Cu^{2+} was the largest in Cu/ceria-Ar, followed by Cu/ceria-Ar, and the least in Cu/ceria-H_2. Understandably, the quantitative relationship of Cu^{2+} emphasizes the easy interaction of Cu^{2+} with oxygen anions (O_L) at lower oxygen vacancy concentrations.

To further accurately confirm the existence form and valence state of copper species, X-ray absorption fine structure spectroscopy (XAFS) was utilized to obtain the valence information and coordination structure of Cu atoms. We normalized and analyzed the Cu K-edge X-ray absorption near edge structure (XANES) of Cu/ceria-H_2. The absorption edge position of Cu/ceria-H_2 was found to be between Cu_2O and CuO, indicating that the Cu valence state was between +1 and +2, preferring +1 (Figure 2f). We can assume when Cu species are incorporated into ceria, Cu^{2+} is connected to lattice oxygen (Cu^{2+}-O_L-Ce^{4+}), while Cu^+ is

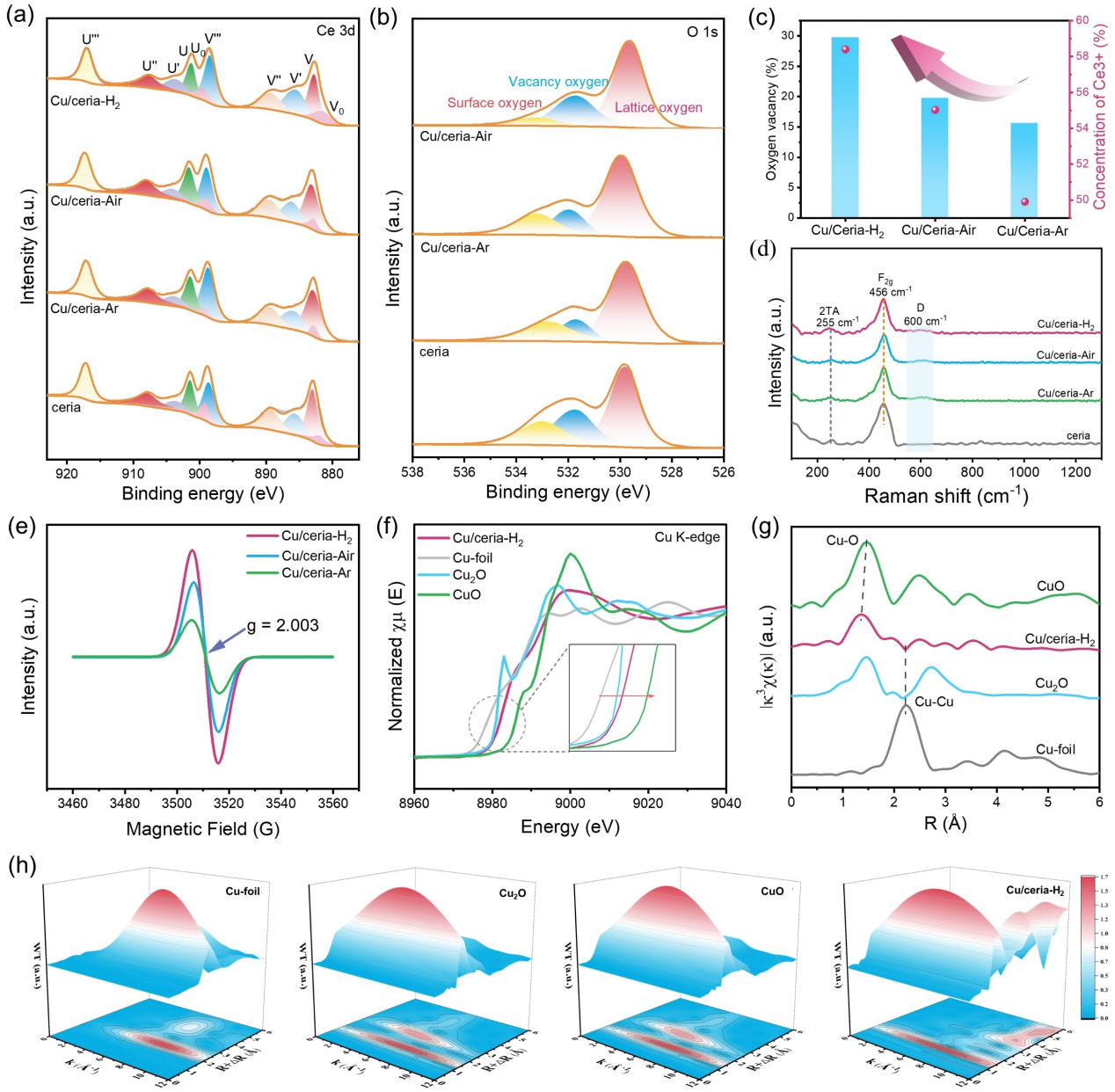

Figure 2. Chemistry and structural characterizations. (a) Ce 3d, (b) O 1s spectra of different samples. (c) Relative concentration of Ce^{3+} and oxygen vacancies present in the Cu/ceria catalysts. (d) Raman spectra of the Cu/ceria catalysts. (e) EPR spectra of the Cu/ceria catalysts. (f) Cu K-edge X-ray absorption near-edge structure (XANES) spectra and (g) extended X-ray absorption fine structure spectroscopy (EXAFS) spectra of Cu/ceria-H_2 and reference samples. (h) Wavelet transform (WT) images of the EXAFS spectra of the Cu-foil, Cu_2O, CuO, and Cu/ceria-H_2.

linked with vacant oxygen (Cu^+-O_v-Ce^{3+}).[29] The relationship between Ce^{3+}, oxygen vacancy, and Cu^+ indicates that various calcination atmospheres can govern the Cu^+ sites in Cu/ceria catalysts, with the oxygen vacancy contributing to the stabilization of Cu^+. The Fourier transform analysis of the κ^3-weighted extended X-ray absorption fine structure (EXAFS) spectra for these samples was presented in Figure 2g. The peak at 1.44 Å in Cu/ceria-H_2 was attributed to the existence of Cu–O bond, while no peak of Cu–Cu bond occurs at 2.44 Å, indicating that the single-atom characteristic of Cu species. The coordination structure information of the sample was obtained by quantitative FT-EXAFS (Figures S13–S15 and Table S5). The O coordination number of Cu in Cu/ceria-H_2 was 2.92 ± 1.02, which supports the presence of oxygen vacancies and follows the DFT calculation model. Additionally, the wavelet transform (WT) of XANES in k-space further confirmed that Cu exists as a single atom (Figure 2h).

2.2. The ECO_2RR Performance of Catalysts

The ECO_2RR performance of Cu/ceria catalysts and related materials was investigated in a flow cell under 1.0 M KOH

electrolyte (Figure S16). The gaseous and liquid products of electrochemical CO_2 reduction were quantitatively analyzed by online gas chromatography (GC, Figure S17) and nuclear magnetic resonance (NMR, Figure S20), respectively. To verify the role of Cu species in the catalytic reaction, FEs of pure ceria were tested and results showed ceria performed almost a hydrogen evolution reaction (HER) with minimal selectivity towards CH_4 (Figure S21). In the contrast, copper doping could significantly enhances the selective production of CH_4, suggesting that Cu served as the active site for the electrocatalytic CO_2 to CH_4.[22a]

We probed the effect of oxygen vacancy concentration on ECO_2RR activity. The linear sweep voltammetry (LSV) curve in Figure 3a showed that Cu/ceria-H_2 had a higher current density than Cu/ceria-Air and Cu/ceria-Ar in the whole potential window, indicating an improved CO_2 reduction capacity on the Cu/ceria-H_2 catalyst.[24] The Faraday efficiencies of the three Cu/ceria catalysts were tested within the potential range of −1.09 V to −1.59 V vs. RHE (Figures 3b–d and Figure S22). The Cu/ceria-H_2 observed a higher FE_{CH4} than Cu/ceria-Air and Cu/ceria-Ar, while the FE_{H2} was lower than Cu/ceria-Air and Cu/ceria-Ar (Figures S23–S24). All the contact angles of the three Cu/ceria catalysts were greater than 90°, implying the Cu/ceria-H_2 had the superior hydrophobicity with the weak HER performance (Figure S25). Interestingly, the maximum FE_{CH4} of Cu/ceria-H_2 was up to 70.03 %, much higher than Cu/ceria-Air (47.11 %) and Cu/ceria-Ar (39.91 %) at −1.49 V vs. RHE,[30] suggesting the increased oxygen vacancies concentration in the Cu/ceria catalyst enhanced the selectivity for the electrochemical ECO_2RR to CH_4 and suppressed the competing HER.

Subsequently, the product selectivity of Cu/ceria-H_2 with varying copper contents was also investigated. The results showed the selectivity of CH_4 initially increased and then decreased as the Cu doping content gradually increased (Figure S26), and the methane activity was the best when the loading 4 wt % (ICP measured actual content ~1 %). Additionally, we investigated the impact of electrolyte concentration on catalyst performance and found that a 1.0 M KOH solution yielded the best results (Figure S27).

Moreover, the conversion frequency (TOF) of CH_4 produced by Cu/ceria catalysts were calculated to reflect the intrinsic activity of the catalysts.[6,10c] The Cu/ceria-H_2 catalyst recorded the highest CH_4 conversion frequency, up to 9946.7 h^{-1} (Figure S28a). The CO_2-to-CH_4 conversion rate of Cu/ceria-H_2 was 0.141 μmol cm^{-2} s^{-1},[31] which was 1.6 and 2.1 times higher than Cu/ceria-Air (0.088) and Cu/ceria-Ar (0.067), respectively (Figure S28b). To investigate the long-term stability of the three catalysts, we performed the chronoamperometry test at −1.49 V vs. RHE. The Cu/ceria-H_2 demonstrated the best durability during the 450 minutes, maintaining a constant current density of approximately −148 mA cm^{-2}. The FE_{CH4} remained above 60 % throughout the test processes, indicating the excellent stability for Cu/ceria-H_2 catalyst (Figure S29). The overall performance of three Cu/ceria catalysts at −1.49 V vs. RHE was shown in Figure 3e. The Cu/ceria-H_2 exhibits the largest shape area, demonstrating the best performance among the three catalysts.[13] More importantly, the FE_{CH4} and current density over Cu/ceria-H_2 had already surpassed those of many recently reported Cu-based catalysts (Figure 3f and Table S6).

The physical properties of Cu/ceria-H_2 after the reaction were investigated. Figure 4a showed that the catalyst underwent a minimal phase transition. The elemental composition and valence state of Cu/ceria-H_2 after catalytic process were analyzed by XPS. Compared to the pre-catalytic process, more elements F, N, K and S appeared, which was attributed to the residual electrolyte and the presence of Nafion bonding agent (Figure 4b). Then, it could be seen from the Figure 4c that the Ce^{3+} content increased after ECO_2RR, indicating that fractional Ce^{4+} was reduced to Ce^{3+} during the electrochemical reaction. At the same time, the amount of lattice oxygen in the catalyst decreased and the surface oxygen increased, which may be the influence of the O element in the Nafion reagent. The observed a small change in the amount of vacancy oxygen, suggesting it may stabilize Cu^+ during the catalytic reaction (Figure 4d). Then, the valence state of Cu was shown in Figure S30, where the peak of Cu^+ (571.52 eV) can be found.[10a,28] Moreover, the Cu/ceria-H_2 after the reaction retained its original sheet-like structure (stack of nanorods) and lattice fringes, and the elements distribution showed uniform distribution without copper aggregation (Figures 4e–g). The stability of the morphology and properties after catalytic reaction was

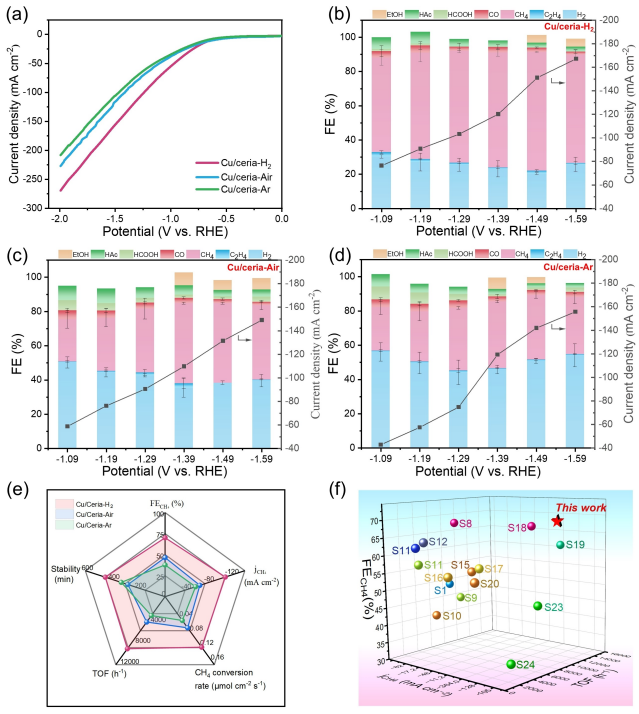

Figure 3. ECO_2RR-to-CH_4 performance. (a) Linear sweep voltammetry (LSV) curves in 1 M KOH aqueous solution in CO_2 atmosphere. ECO_2RR product selectivity and current densities on the (b) Cu/ceria-H_2, (c) Cu/ceria-Air, (d) Cu/ceria-Ar. (e) Overall ECO_2RR performance evaluation at −1.49 V vs. RHE. (f) Comparison of CH_4 selectivity, partial current density, and TOF values with those of recently reported electrocatalysts.

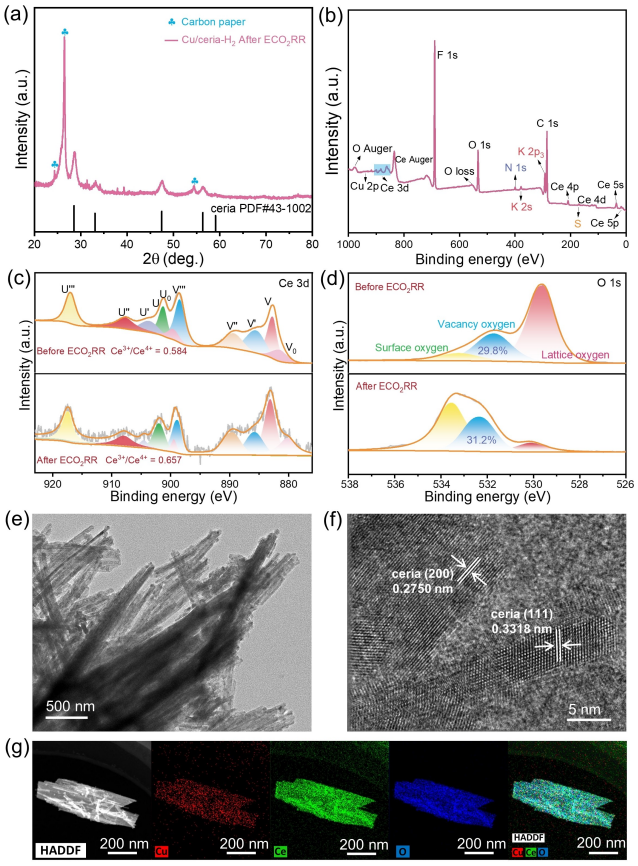

Figure 4. Structure characterizations of Cu/ceria-H_2 after ECO_2RR. (a) XRD patterns of Cu/ceria-H_2 on carbon paper after ECO_2RR. (b) XPS spectrum of Cu/ceria-H_2 after ECO_2RR. (c) Ce 3d, (d) O 1s spectra for Cu/ceria-H_2 after ECO_2 RR. (e) TEM, (f) HR-TEM, (g) HAADF-TEM and EDS elemental mapping images for Cu/ceria-H_2 after ECO_2RR.

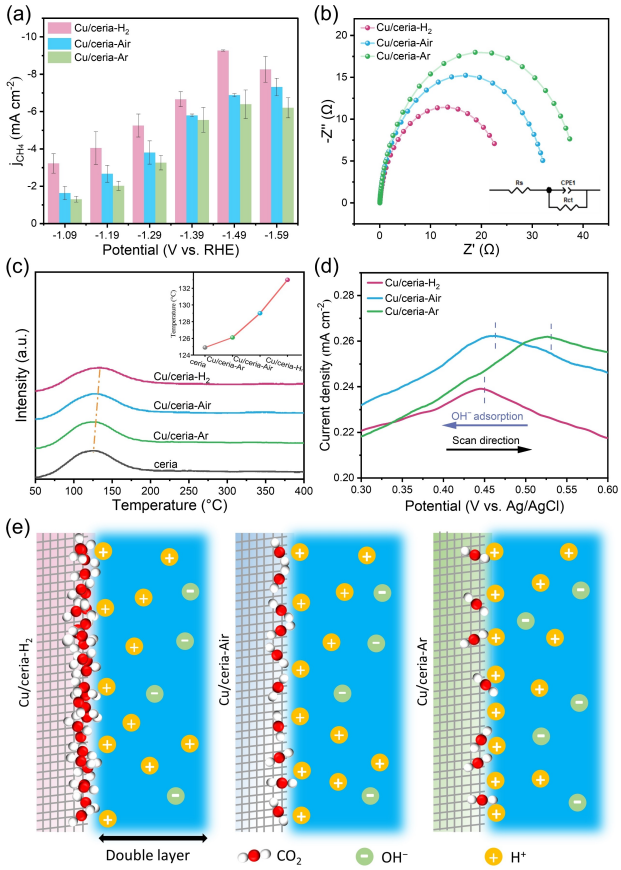

Figure 5. Mechanistic investigation of the intrinsic activity. (a) Methane partial current density normalized to a double-layer capacitor. (b) Nyquist plots over the frequency ranging from 10^5 to 0.01 Hz. (c) CO_2 TPD curves of the catalysts. (d) Single oxidative LSV scans of different samples at 50 mV s^{-1} in Ar-saturated 0.1 M KOH. (e) Three Cu/ceria catalysts for CO_2 adsorption capacity diagram.

attributed to the modulation of the oxygen vacancies around the copper.

2.3. Mechanism of the Intrinsic Catalytic Activity

To investigate the possible origin for the improved ECO_2RR performance, the contribution of electrochemical active surface area (ECSA) to the catalytic activity was first assessed.[32] The methane local current density obtained by the double layer capacitance normalization was used to evaluate the inherent activity of the catalyst. Using cyclic voltammetry curves at different sweeping speeds, the double layer capacitance values of Cu/ceria-H_2, Cu/ceria-Air, and Cu/ceria-Ar were calculated to be 0.91 mF/cm^2, 0.71 mF/cm^2, and 0.67 mF/cm^2, respectively (Figure S31), which in turn showed that Cu/ceria-H_2 has the best ECSA. Meanwhile, Figure 5a showed the best methane-normalized current density of Cu/ceria-H_2 in a certain potential range.It was evident that the oxygen vacancy enhanced the intrinsic activity of the Cu/ceria catalyst against ECO_2RR. Additionally, the electrochemical impedance spectroscopy (EIS) was utilized to study the electron transfer kinetics of the catalytic reaction.[6] Oxygen vacancies could boost the charge transfer rate of the electrocatalytic reaction, as evidenced by the lowest charge transfer resistance (R_{ct}) for Cu/ceria-H_2 in Figure 5b.

We also explored the possible reasons for the superior catalytic activity in terms of the CO_2 molecules adsorption strength of the catalyst. The CO_2 temperature programmed desorption (TPD) diagram reflected the adsorption capacity of the catalyst for CO_2.[7a,22b] The Cu/ceria-H_2 catalyst presents the highest CO_2 desorption peak, indicating that oxygen vacancies could promote the adsorption of CO_2 (Figure 5c). Due to $*CO_2^{\bullet-}$ was unstable in electrolyte, OH^- adsorption was determined by mono-oxidation LSV to observe the $*CO_2^{\bullet-}$ content on the catalyst.[15a,33] Cu/ceria-H_2 exhibited a lower potential for OH^- adsorption (0.445 V) compared to Cu/ceria-Air (0.463 V) and Cu/ceria-Ar (0.526 V) (Figure 5d). The results demonstrated that Cu/ceria-H_2 had the most favorable binding ability to $*CO_2^{\bullet-}$, which was facile to activate CO_2. Therefore, as the number of oxygen vacancies increased, Cu/ceria-H_2 exhibited a distinct ECSA and CO_2 adsorption capacity combined with

faster charge transfer and kinetics, thus improving the activity of the CH_4 product (Figure 5e).

2.4. DFT Calculations and Operando ATR-SEIRAS Characterization

Density functional theory (DFT) calculation was further employed to unveil the role of oxygen vacancy concentration on the methane selectivity. Based on the previous characterizations, the order of oxygen vacancy concentration of Cu/ceria catalyst under three different atmospheres follows the sequence of Cu/ceria-H_2 > Cu/ceria-Air > Cu/ceria-Ar. In the Cu/ceria-H_2 calculation model, the oxygen vacancy number was set to 3. The oxygen vacancy number of Cu/ceria-Air and Cu/ceria-Ar were set to be 2 and 1 respectively, and the corresponding calculation model was shown in (Figure S32). The ECO_2RR usually occurs by the adsorption of CO_2 molecules on the catalyst surface, followed by the formation of $*CO_2^{\bullet-}$ with electrons, and then the subsequent protonation. Given the importance of this step, the adsorption energy and corresponding average bond length of CO_2 adsorbed on the three catalysts (Figure S33) were calculated. Compared to Cu/ceria-Air (−0.28 eV) and Cu/ceria-Ar (−0.20 eV), the smallest CO_2 adsorption energy on the Cu/ceria-H_2 (−0.42 eV) surface suggested that the high oxygen vacancy number around single-atom copper could efficiently adsorb CO_2 and form an efficient activation catalytic center to promote the activation of CO_2.[21a,24]

Based on the bader charge analysis, the charge of the C atom in CO_2 was 3.14 |e| on Cu/ceria-H_2, 2.99 |e| on Cu/ceria-Air, and 2.66 |e| on Cu/ceria-Ar. This indicated that the electron density of the Cu/ceria-H_2 catalyst surface was the highest. It could be concluded that catalysts with a higher number of oxygen vacancies had a stronger electron supply capability, which was beneficial for the activation and reduction of CO_2, promoting the C atom to gain more electrons (Figure S34).[24] The charge difference distribution demonstrated the electronic interaction between the *COOH intermediate and the three catalysts (Figures 6a–c and Figure S35). The Cu/ceria-H_2 transferred more charge to *COOH compared to Cu/ceria-Air and Cu/ceria-Ar. The Cu/ceria-H_2 exhibited a stronger interaction with *COOH and a higher number of electron transfers, indicating the higher surface activity.

Each reaction step with the Gibbs free energy of the methane formation paths for the three catalysts were calculated. The total path was $*+CO_2 \rightarrow *COOH \rightarrow *CO \rightarrow *CHO \rightarrow *CHOH \rightarrow *CH_3O \rightarrow *O + CH_4$ (Figure 6d). The intermediate and reaction path diagrams of the multi-stage electrocatalytic methane production reaction with Cu/ceria catalysts were shown in Figure S35. Initially, the reaction free energy change of CO_2 hydrogenation to form *COOH were compared. The Gibbs free energies of Cu/ceria-H_2, Cu/ceria-Air, and Cu/ceria-Ar were −1.12, −0.74, and −0.84 eV, respectively, indicating that the formation of *COOH was a spontaneous exothermic process, and the protonation of Cu/ceria-H_2 to *COOH was the most favorable process.

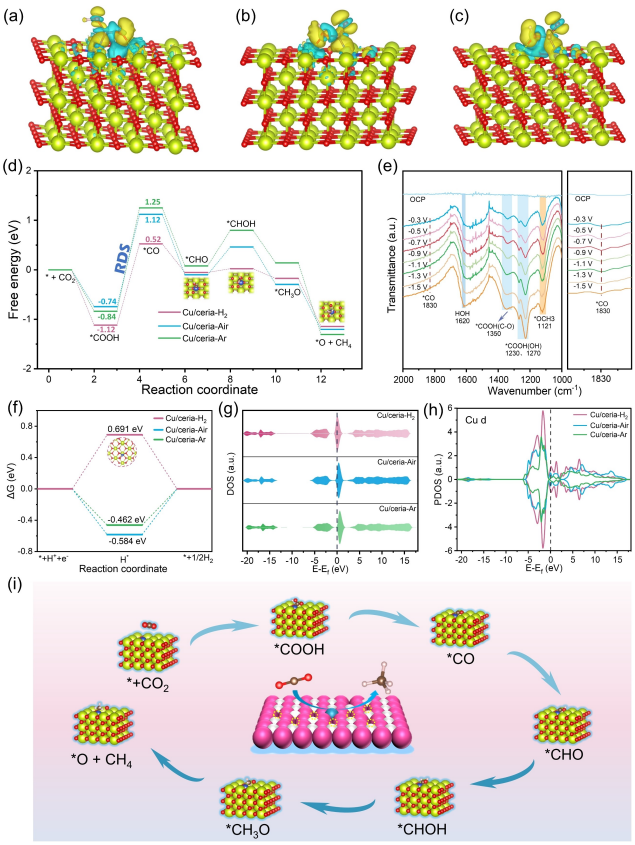

Figure 6. Relationship between ECO_2RR selectivity and the oxygen vacancies at Cu sites. (a–c) Charge density difference of *COOH over Cu/ceria-H_2, Cu/ceria-Air and Cu/ceria-Ar catalysts. The isosurface level was set to 0.003 au, depicting charge depletion and accumulation in cyan and yellow, respectively. (d) Gibbs free energy profiles for the CO_2 reduction to CH_4 reaction pathway. (e) Operando ATR-SEIRAS spectra on Cu/ceria-H_2 at different potentials in CO_2-saturated 0.5 M $KHCO_3$ electrolyte. (f) Gibbs free energy diagram for HER on Cu/ceria-H_2, Cu/ceria-Air and Cu/ceria-Ar catalysts. (g) Density of states (DOS) of Cu/ceria catalysts. The dotted line represents the Fermi energy level. (h) Partial density of states (PDOS) of Cu atom d state in Cu/ceria catalysts. The dotted line represents the Fermi energy level. (i) The reaction pathway mechanism of ECO_2RR to CH_4 products was proposed.

Furthermore, the further protonation of *COOH to form *CO represented the most challenging non-spontaneous process along the entire reaction pathway, indicating that the rate-determining step (RDS) of CH_4 generation was *COOH-to-*CO. The free energy change for the RDS on Cu/ceria-H_2 was 1.64 eV, which was 0.22 eV lower than that on Cu/ceria-Air and 0.45 eV lower than that on Cu/ceria-Ar. This suggested that Cu/ceria-H_2 reduced the free energy for *COOH-to-*CO conversion, resulting in faster initial kinetics, making it more favorable for subsequent protonation to produce CH_4. Simultaneously, the ΔG for *H intermediate formation involved in HER on Cu/ceria-H_2 was the largest among the three Cu/ceria catalyst, indicating that the Cu/ceria-H_2 catalyst had a better inhibition effect on the

HER (Figure 6f).[34] Because *H also adsorbs at the Cu site, and more oxygen vacancies lower the adsorption of *H, thus inhibiting the occurrence of HER.

In parallel, to further clarify the reaction intermediates and possible reaction pathways of ECO_2RR, we performed operando ATR-SEIRAS tests for Cu/ceria-H_2 and Cu/ceria-Ar (Figure S36a). Initially, the peaks observed between 1230 cm^{-1} and 1270 cm^{-1} were identified as O–H deformation of the *COOH group, while the peaks at 1350 cm^{-1} were attributed to C–O bond stretching of the *COOH group (Figure 6e and Figure S37).[15b] The peak strength of Cu/ceria-H_2 at these two locations was greater than those of Cu/ceria-Ar, indicating that the adsorption capacity of *COOH was stronger, with more protonation into *CO,[35] which was consistent with the results of the step diagram. Secondly, Cu/ceria-H_2 has a much stronger *CO peak at 1820 cm^{-1} than Cu/ceria-Ar,[36] showing that more oxygen vacancies contributed to the better adsorption capacity for *CO. Third, the strong adsorption of Cu/ceria-H_2 to *CO facilitated the formation of $*CH_3O$ (1121 cm^{-1}) as an important intermediate for CH_4 production.[37]

Moreover, we calculated the density of states (DOS) for the three Cu/ceria catalysts and found that all three exhibited a band at the Fermi level, with the Cu/ceria-H_2 showing the largest band area at the Fermi level, while the Cu/ceria-Ar had the smallest (Figure 6g). The electronic states near the Fermi level are more likely to participate in electrical conduction, and the presence of more electronic states at the Fermi level in the Cu/ceria-H_2 catalyst suggests its potential higher conductivity and the ability of the catalyst to provide electrons to the adsorption intermediate.[21a,38] To confirm the electrical conductivity of these three Cu/ceria catalysts, we measured their V–I curves using the four-probe method at 298 K (Figure S38).[39] The electronic conductivities of Cu/ceria-Air and Cu/ceria-Ar were 8.82×10^{-6} $S\,m^{-1}$ and 1.65×10^{-6} $S\,m^{-1}$, respectively, both lowered than that of Cu/ceria-H_2 (5.94×10^{-5} $S\,m^{-1}$) (Figure S39 and Table S7).

Additionally, the partial density of states (PDOS) for the copper orbitals showed that Cu/ceria-H_2 had the highest density of states, indicating that Cu/ceria-H_2 had more available electronic states within a certain energy range (Figure 6h).[21a,40] Figure S40 showed that the p state of O of Cu/ceria-H_2 catalyst overlaps more obviously near the Fermi level and the contribution of f state of Ce was enhanced at the Fermi level, indicating that oxygen vacancies regulated the interaction between Cu and Ce sites and changed the local electronic environment of Cu atoms. Figure S41 showed that the bader charge of Cu in Cu/ceri-H_2 catalyst was -1.06 $|e|$, which was smaller than that of Cu/ceri-Air (-0.82 $|e|$) and Cu/ceri-Ar (-0.70 $|e|$), indicating that oxygen vacancies led to an increase in the electron density of the Cu site and a more negative charge of the Cu site.The higher concentration of oxygen vacancies in Cu/ceria catalysts increases the electron transfer capacity, which was more favorable for the participation of active sites (copper atom) in the ECO_2RR reaction.

At the same time, we constructed a 2Cu/ceria-H_2 model with two Cu active sites to further calculate the Gibbs free energy distribution of CH_4 generation (Figure S42). It was found that the energy barrier of 2Cu/ceria-H_2 was higher for the same RDS step (Figure S43), indicating that there was no synergy between multiple single Cu active sites. Here, the total path and mechanism of the Cu/ceria-H_2 electrocatalytic reaction to produce methane was illustrated in Figure 6i. The above theoretical calculations and operando experiments results suggested that Cu/ceria-H_2 has strong electron supply ability and conduction ability, which was conducive to the activation and reduction of CO_2, promoting *COOH to the formation of *CO with less energy. Thus, it exhibited stronger reaction activity, endowing a better catalytic effect, which was in agreement with the higher CH_4 selectivity of Cu/ceria-H_2.

3. Conclusions

In conclusion, we prepared Cu monoatomic site catalysts to stabilize the oxygen vacancy on ceria by atmosphere-assisted thermal treatment strategy. Quantitative analysis of oxygen vacancies by XPS, Raman and EPR characterizations proved that the Cu/ceria-H_2 catalysts possess more oxygen vacancies than those with air and Ar atmosphere. The relationship between the oxygen vacancy concentration and the ECO_2RR performance was revealed by systematic experiments and calculations. The Cu/ceria-H_2 with the highest oxygen vacancies manifests the best electrochemical selectivity toward CH_4, harvesting a 70.03 % Faradaic efficiency and 9946.7 h^{-1} turnover frequency at -1.49 V vs. RHE. Theoretical calculations and operando characterizations indicate that the rich oxygen vacancies can enhance the activation of CO_2, facilitate charge transfer, lower the formation energy barrier of *COOH intermediates, thereby improving the ECO_2RR effect. Our research offers a feasible way for manipulating the electronic structure of SACs onto metal oxides, and plays a pivotal role in the deep exploration of structure-capability correlation of the CO_2 electroreduction to target products.

Acknowledgements

This work was supported by the Guangxi Science and Technology Base and Talent Special Project (GuikeAD23026311), the Natural Science Foundation of Guangxi Province (2024GXNSFAA010271), the National Natural Science Foundation of China (22308066), and the Opening Project of Guangxi Key Laboratory of Petrochemical Resource Processing and Process Intensification Technology (2023 K007). We also acknowledge the National High-Performance Computing Center Nanning Branch and Multi-functional Computer Center of Guangxi University for providing access to supercomputer resources. The authors would like to thank Jianliang Liao from Shiyanjia Lab (www.shiyanjia.com) for the XANES measurement.

Conflict of Interest

The authors declare no conflict of interest.

Data Availability Statement

The data that support the findings of this study are available from the corresponding author upon reasonable request.

Keywords: carbon dioxide electroreduction · ceria · methane · oxygen vacancy concentration · single-atom catalysts

[1] a) Y. Y. Birdja, E. Pérez-Gallent, M. C. Figueiredo, A. J. Göttle, F. Calle-Vallejo, M. T. M. Koper, *Nat. Energy* **2019**, *4*, 732–745; b) J. H. Montoya, L. C. Seitz, P. Chakthranont, A. Vojvodic, T. F. Jaramillo, J. K. Nørskov, *Nat. Mater.* **2016**, *16*, 70–81.

[2] M. Esmaeilirad, A. Kondori, B. Song, A. Ruiz Belmonte, J. Wei, K. Kucuk, S. M. Khanvilkar, E. Efimoff, W. Chen, C. U. Segre, R. Shahbazian-Yassar, M. Asadi, *ACS Nano* **2020**, *14* (2), 2099–2108.

[3] S. Chen, Y. Su, P. Deng, R. Qi, J. Zhu, J. Chen, Z. Wang, L. Zhou, X. Guo, B. Y. Xia, *ACS Catal.* **2020**, *10*, 4640–4646.

[4] S. Zhu, E. P. Delmo, T. Li, X. Qin, J. Tian, L. Zhang, M. Shao, *Adv. Mater.* **2021**, *33*, e2005484.

[5] Z. Han, Y. Zhengwu, K. Xiangdong, G. Zhigang, Z. Jie, *Chin. J. Catal.* **2022**, *7*, 1634–1641.

[6] L. Xue, C. Zhang, J. Wu, Q.-Y. Fan, Y. Liu, Y. Wu, J. Li, H. Zhang, F. Liu, S. Zeng, *Appl. Catal. B* **2022**, *304*, 120951.

[7] a) J. Yin, Z. Gao, F. Wei, C. Liu, J. Gong, J. Li, W. Li, L. Xiao, G. Wang, J. Lu, L. Zhuang, *ACS Catal.* **2022**, *12*, 1004–1011; b) S. B. Varandili, J. Huang, E. Oveisi, G. L. De Gregorio, M. Mensi, M. Strach, J. Vavra, C. Gadiyar, A. Bhowmik, R. Buonsanti, *ACS Catal.* **2019**, *9*, 5035–5046; c) S. Chu, X. Yan, C. Choi, S. Hong, A. W. Robertson, J. Masa, B. Han, Y. Jung, Z. Sun, *Green Chem.* **2020**, *22*, 6540–6546; d) H.-D. Cai, B. Nie, P. Guan, Y.-S. Cheng, X.-D. Xu, F.-H. Wu, G. Yuan, X.-W. Wei, *ACS Appl. Nano Mater.* **2022**, *5*, 7259–7267.

[8] S. Hong, H. G. Abbas, K. Jang, K. K. Patra, B. Kim, B. U. Choi, H. Song, K. S. Lee, P. P. Choi, S. Ringe, J. Oh, *Adv. Mater.* **2022**, *35*, 8.

[9] a) J.-F. Xie, J.-J. Chen, Y.-X. Huang, X. Zhang, W.-K. Wang, G.-X. Huang, H.-Q. Yu, *Appl. Catal. B* **2020**, *270*, 118864; b) D. Wang, J. Mao, C. Zhang, J. Zhang, J. Li, Y. Zhang, Y. Zhu, *eScience* **2023**, *3*, 3.

[10] a) K. K. Patra, Z. Liu, H. Lee, S. Hong, H. Song, H. G. Abbs, Y. Kwon, S. Ringe, J. Oh, *ACS Catal.* **2022**, *12*, 10973–10983; b) Y. Wang, Z. Chen, P. Han, Y. Du, Z. Gu, X. Xu, G. Zheng, *ACS Catal.* **2018**, *8*, 7113–7119; c) S. Chen, B. Wang, J. Zhu, L. Wang, H. Ou, Z. Zhang, X. Liang, L. Zheng, L. Zhou, Y. Q. Su, D. Wang, Y. Li, *Nano Lett.* **2021**, *21*, 7325–7331.

[11] a) X. Wang, P. Ou, J. Wicks, Y. Xie, Y. Wang, J. Li, J. Tam, D. Ren, J. Y. Howe, Z. Wang, A. Ozden, Y. Z. Finfrock, Y. Xu, Y. Li, A. S. Rasouli, K. Bertens, A. H. Ip, M. Graetzel, D. Sinton, E. H. Sargent, *Nat. Commun.* **2021**, *12*, 1; b) G. L. De Gregorio, T. Burdyny, A. Loiudice, P. Iyengar, W. A. Smith, R. Buonsanti, *ACS Catal.* **2020**, *10*, 4854–4862.

[12] J. Wang, D. Deng, Q. Wu, M. Liu, Y. Wang, J. Jiang, X. Zheng, H. Zheng, Y. Bai, Y. Chen, X. Xiong, Y. Lei, *ACS Nano* **2023**, *17*, 18688–18705.

[13] Y. Zhang, L.-Z. Dong, S. Li, X. Huang, J.-N. Chang, J.-H. Wang, J. Zhou, S.-L. Li, Y.-Q. Lan, *Nat. Commun.* **2021**, *12*, 1.

[14] Y. Liang, C. Wu, S. Meng, Z. Lu, R. Zhao, H. Wang, Z. Liu, J. Wang, *ACS Appl. Mater.* **2023**, *15*, 30262–30271.

[15] a) Z. Chen, X. Zhang, W. Liu, M. Jiao, K. Mou, X. Zhang, L. Liu, *Energy Environ. Sci.* **2021**, *14*, 2349–2356; b) Y. Zhang, Q. Zhou, Z. F. Qiu, X. Y. Zhang, J. Q. Chen, Y. Zhao, F. Gong, W. Y. Sun, *Adv. Funct. Mater.* **2022**, *32*, 36.

[16] L. Li, Y. Huang, Y. Li, *EnergyChem* **2020**, *2*, 1.

[17] J. A. Rodriguez, D. C. Grinter, Z. Liu, R. M. Palomino, S. D. Senanayake, *Chem. Soc. Rev.* **2017**, *46*, 1824–1841.

[18] A. Jeyaranjan, T. S. Sakthivel, C. J. Neal, S. Seal, *Carbon* **2019**, *151*, 192–202.

[19] K. Zhang, Q. Guo, Y. Wang, P. Cao, J. Zhang, M. Heggen, J. Mayer, R. E. Dunin-Borkowski, F. Wang, *ACS Catal.* **2023**, *5*, 3164–3169.

[20] a) H. Sun, H. Wang, Z. Qu, *ACS Catal.* **2023**, *13* (2), 1077–1088; b) R. Xie, L. Ma, K. Sun, G. Zhou, Z. Qu, N. Yan, *J. Hazard. Mater.* **2021**, *420*, 126545; c) L. Zhang, F. Liu, Y. Yu, Y. Liu, C. Zhang, H. He, *Chin. J. Catal.* **2011**, *32*, 727–735.

[21] a) Y. X. Duan, Y. T. Zhou, Z. Yu, D. X. Liu, Z. Wen, J. M. Yan, Q. Jiang, *Angew. Chem. Int. Ed.* **2021**, *60*, 8798–8802; b) Z. Yang, D. Ji, Z. Li, Z. He, Y. Hu, J. Yin, Y. Hou, P. Xi, C. H. Yan, *Small* **2023**, *19*, e2303099.

[22] a) Y. Zhang, X.-Y. Zhang, W.-Y. Sun, *ACS Catal.* **2023**, *13*, 1545–1553; b) Z. Geng, X. Kong, W. Chen, H. Su, Y. Liu, F. Cai, G. Wang, J. Zeng, *Angew. Chem. Int. Ed.* **2018**, *57*, 6054–6059.

[23] Y. Li, Q. Sun, *Adv. Energy Mater.* **2016**, *6*, 1600463.

[24] Q. Cheng, M. Huang, L. Xiao, S. Mou, X. Zhao, Y. Xie, G. Jiang, X. Jiang, F. Dong, *ACS Catal.* **2023**, *13*, 4021–4029.

[25] T. Ye, W. Huang, L. Zeng, M. Li, J. Shi, *Appl. Catal. B* **2017**, *210*, 141–148.

[26] a) Z. Feng, Q. Ren, R. Peng, S. Mo, M. Zhang, M. Fu, L. Chen, D. Ye, *Catal. Today* **2018**, *332*, 177–182; b) M. Lykaki, E. Pachatouridou, S. A. C. Carabineiro, E. Iliopoulou, C. Andriopoulou, N. Kallithrakas-Kontos, S. Boghosian, M. Konsolakis, *Appl. Catal. B* **2018**, *230*, 18–28; c) Y. Wang, Y. Xue, C. Zhao, D. Zhao, F. Liu, K. Wang, D. D. Dionysiou, *Chem. Eng. J.* **2016**, *300*, 300–305.

[27] a) B. Wang, H. Zhang, W. Xu, X. Li, W. Wang, L. Zhang, Y. Li, Z. Peng, F. Yang, Z. Liu, *ACS Catal.* **2020**, *10* (21), 12385–12392; b) R. A. C. Amoresi, R. C. Oliveira, N. L. Marana, P. B. de Almeida, P. S. Prata, M. A. Zaghete, E. Longo, J. R. Sambrano, A. Z. Simões, *ACS Appl. Nano Mater.* **2019**, *2*, 6513–6526.

[28] J. Ma, F. Huang, A. Xu, D. Wei, X. Chen, W. Zhao, Z. Chen, X. Yin, J. Zhu, H. He, J. Xu, *Adv. Sci.* **2024**, *11*, e2306858.

[29] A. Chen, X. Yu, Y. Zhou, S. Miao, Y. Li, S. Kuld, J. Sehested, J. Liu, T. Aoki, S. Hong, M. F. Camellone, S. Fabris, J. Ning, C. Jin, C. Yang, A. Nefedov, C. Wöll, Y. Wang, W. Shen, *Nat. Catal.* **2019**, *2*, 334–341.

[30] a) T. Zhao, J. Li, J. Liu, F. Liu, K. Xu, M. Yu, W. Xu, F. Cheng, *ACS Catal.* **2023**, *13*, 4444–4453; b) A. Xu, D. Wei, X. Chen, T. Yang, Y. Huang, H. He, J. Xu, *Chem. Eng. J.* **2023**, *452*, 139227.

[31] a) Y. Li, A. Xu, Y. Lum, X. Wang, S.-F. Hung, B. Chen, Z. Wang, Y. Xu, F. Li, J. Abed, J. E. Huang, A. S. Rasouli, J. Wicks, L. K. Sagar, T. Peng, A. H. Ip, D. Sinton, H. Jiang, C. Li, E. H. Sargent, *Nat. Commun.* **2020**, *11*, 1; b) X. Wang, A. Xu, F. Li, S.-F. Hung, D.-H. Nam, C. M. Gabardo, Z. Wang, Y. Xu, A. Ozden, A. S. Rasouli, A. H. Ip, D. Sinton, E. H. Sargent, *J. Mater. Chem. A* **2020**, *142*, 3525–3531; c) C.-J. Chang, S.-C. Lin, H.-C. Chen, J. Wang, K. J. Zheng, Y. Zhu, H. M. Chen, *J. Mater. Chem. A* **2020**, *142*, 12119–12132.

[32] F. Lei, W. Liu, Y. Sun, J. Xu, K. Liu, L. Liang, T. Yao, B. Pan, S. Wei, Y. Xie, *Nat. Commun.* **2016**, *7*, 1.

[33] Z. Chen, G. Yu, B. Li, X. Zhang, M. Jiao, N. Wang, X. Zhang, L. Liu, *ACS Catal.* **2021**, *11*, 14596–14604.

[34] a) X. Zhong, S. Liang, T. Yang, G. Zeng, Z. Zhong, H. Deng, L. Zhang, X. Sun, *ACS Nano* **2022**, *16*, 19210–19219; b) W. Ren, X. Tan, J. Qu, S. Li, J. Li, X. Liu, S. P. Ringer, J. M. Cairney, K. Wang, S. C. Smith, C. Zhao, *Nat. Commun.* **2021**, *12*, 1449.
[35] X. Zhou, J. Shan, L. Chen, B. Y. Xia, T. Ling, J. Duan, Y. Jiao, Y. Zheng, S.-Z. Qiao, *J. Mater. Chem. A* **2022**, *144*, 2079–2084.
[36] a) X. Li, Y. Sun, J. Xu, Y. Shao, J. Wu, X. Xu, Y. Pan, H. Ju, J. Zhu, Y. Xie, *Nat. Energy* **2019**, *4*, 690–699; b) S. Chen, W. H. Li, W. Jiang, J. Yang, J. Zhu, L. Wang, H. Ou, Z. Zhuang, M. Chen, X. Sun, D. Wang, Y. Li, *Angew. Chem. Int. Ed.* **2021**, *61*, 4.
[37] L. Han, X. Liu, J. He, Z. Liang, H. T. Wang, S. M. Bak, J. Zhang, A. Hunt, I. Waluyo, W. F. Pong, J. Luo, Y. Ding, R. R. Adzic, H. L. Xin, *Adv. Energy Mater.* **2021**, *11*, 24.
[38] B. Zhang, J. Zhang, F. Zhang, L. Zheng, G. Mo, B. Han, G. Yang, *Adv. Funct. Mater.* **2019**, *30*, 1906194.
[39] a) M. Liu, S. Yang, X. Yang, C. X. Cui, G. Liu, X. Li, J. He, G. Z. Chen, Q. Xu, G. Zeng, *Nat. Commun.* **2023**, *14*, 3800; b) H. J. Zhu, D. H. Si, H. Guo, Z. Chen, R. Cao, Y. B. Huang, *Nat. Commun.* **2024**, *15*, 1479.
[40] S.-F. Hung, A. Xu, X. Wang, F. Li, S.-H. Hsu, Y. Li, J. Wicks, E. G. Cervantes, A. S. Rasouli, Y. C. Li, M. Luo, D.-H. Nam, N. Wang, T. Peng, Y. Yan, G. Lee, E. H. Sargent, *Nat. Commun.* **2022**, *13*, 819.

Manuscript received: August 15, 2024
Accepted manuscript online: September 23, 2024
Version of record online: November 2, 2024